# Theoretical Study of POCOP-Pincer Iridium(III)/Iron(II) Hydride Catalyzed Hydrosilylation of Carbonyl Compounds: Hydride Not Involved in the Iridium(III) System but Involved in the Iron(II) System

Wenmin Wang, Piao Gu, Yiou Wang, and Haiyan Wei*

Jiangsu Key Laboratory of Biofunctional Materials, School of Chemistry and Materials Science, Jiangsu Provincial Key Laboratory for NSLSCS, Nanjing Normal University, Nanjing 210097, People's Republic of China

Ⓢ Supporting Information
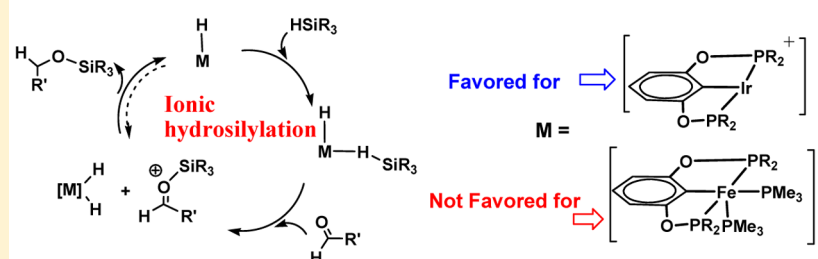
ABSTRACT: The catalytic hydrosilylation of carbonyl compounds by two POCOP-pincer transition-metal hydrides, $(POCOP)Ir(H)(acetone)^+$ (**1A-acetone**) and $(POCOP)Fe(H)(PMe_3)_2$ (**1B**) (POCOP = 2,6-bis(dibutyl-/diisopropylphosphinito)phenyl), was theoretically investigated to determine the underlying reaction mechanism. Several plausible mechanisms were analyzed using density functional theory calculations. The **1A-acetone**-catalyzed hydrosilylation of carbonyl compounds proceeds via the ionic hydrosilylation pathway, which is initiated by the nucleophilic attack of the η^1-silane metal adduct by carbonyl substrate. This attack results in the heterolytic cleavage of the Si−H bond and the generation of a siloxy carbenium ion paired with a neutral iridium dihydride, $[(POCOP)Ir(H)_2][R_3SiOCHR']^+$, followed by transfer of hydride from the metal center to the siloxy carbenium ion to yield the silyl ether product. The activation energy of the turnover-limiting step was calculated as ∼15.2 kcal/mol. This value is energetically more favorable than those of other pathways by as much as 22.6 kcal/mol. The most energetically favorable process for the hydrosilylation of carbonyl compound catalyzed by POCOP-pincer iron hydride **1B** was determined as the carbonyl precoordination pathway, which involves the initial coordination of the carbonyl substrate to the metal center and subsequent migratory insertion into the M−H bond to give the alkoxide intermediate. This intermediate then undergoes M−O/Si−H σ-bond metathesis to yield the silyl ether product. The ionic hydrosilylation pathway requires an activation energy that is ∼30.0 kcal/mol higher than that of the carbonyl precoordination pathway. Our calculation results indicate that the hydride moiety is not involved in the POCOP-pincer iridium(III) hydride **1A-acetone**-catalyzed hydrosilylation of carbonyl compounds but is involved in the POCOP-pincer iron(II) hydride **1B**-catalyzed process.

■ INTRODUCTION

Transition-metal hydride species are important compounds used in a wide range of catalytic and stoichiometric processes.[1−9] Moreover, transition-metal hydrides are often produced as key intermediates in a variety of catalytic reactions. For example, in the generally accepted Chalk−Harrod mechanism, which has been proposed to account for the hydrosilylation reaction of unsaturated substrates catalyzed by low-valent transition-metal complexes, the key step is the generation of a metal silyl hydride by the oxidative addition of silane to the metal center (Scheme 1a).[10,11] In addition, the recently proposed [2 + 2] addition mechanism explains the hydrosilylation of carbonyl compounds catalyzed by high-valent transition-metal complexes, such as $Re(O)_2I(PPh_3)_2$,[12] MoO_2Cl_2,[13] and others.[14] The key step in this mechanism is the addition of a Si−H bond across one of the Re/Mo=O

Scheme 1
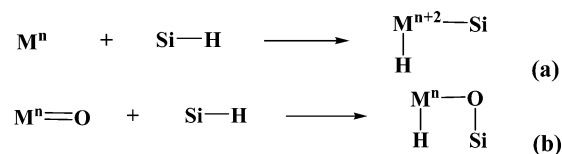
bonds in a [2 + 2] fashion to generate the hydrido−oxo intermediate $Re(O)(OSiR_3)(H)I(PPh_3)_2$ or $Mo(O)(OSiR_3)(H)Cl_2$ (Scheme 1b).[15] The generated transition-metal hydrides in Scheme 1 are postulated as the key intermediates in the subsequent catalytic transformation cycles, which occur

via migratory insertion of the carbonyl compounds into the M—H bond. Therefore, both hydrosilylation mechanisms involved the process of insertion of the metal—hydride bond into the carbonyl compounds.

However, an alternative mechanistic model has been proposed recently that is based on donation of a hydride by the transition-metal catalyst to an appropriate electrophile to complete the reduction reaction.[16−18] In this model, the mechanistic requirement for the coordination of the unsaturated carbonyl species is unnecessary, thus widening the range of transition metals that can be used. Recently, Brookhart and co-workers[19] reported that the highly electrophilic POCOP-pincer iridium hydride (POCOP)Ir(H)(acetone)$^+$ (**1A-acetone**) can efficiently catalyze the hydrosilylation of ketones/aldehydes. In addition, the catalytic reaction is believed to proceed via the aforementioned alternative mechanistic pathway. As shown in Scheme 2, the proposed catalytic cycle

Scheme 2
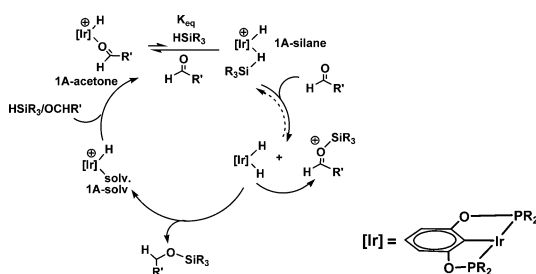
consists of three steps: (1) the binding of silane to the electrophilic iridium center to form an η^1-silane transition-metal complex (**1A-silane**), which is in equilibrium with the ketone complex of **1A-acetone**, (2) the transfer of the silyl ion (R$_3$Si$^+$) of the η^1-silane transition-metal complex (**1A-silane**) to the carbonyl substrate to produce the oxocarbonium ion [R$_3$SiOCHR']$^+$, and (3) the reduction of the oxocarbonium ion by the resultant iridium dihydride to yield the silyl ether product.

The catalytic cycle for the hydrosilylation of carbonyl compounds by **1A-acetone** (Scheme 2) resembles that of a previously postulated scheme for catalytic hydrosilylation reactions with the Lewis acid B(C$_6$F$_5$)$_3$.[20] The catalytic mechanism, called the ionic hydrosilylation mechanism, involves the sequential transfer of a silyl ion (R$_3$Si$^+$) and then a hydride to a polar double bond to furnish the reduction products.[21] Therefore, an important mechanistic distinction between the traditional catalysts (Scheme 1) and the ionic hydrogenation/hydrosilylation catalysts (Scheme 2) involves the coordination of the unsaturated substrate to the metal center. Neither the coordination of unsaturated substrate to the metal center nor its insertion into the M—H bond is involved in an ionic mechanism. Removing the requirement for substrate coordination and its subsequent insertion widens the range of transition metals that can be used. Therefore, the catalysts involved in the ionic mechanism have drawn considerable attention.

Recently, Guan and his collaborators reported the use of an analogous POCOP-pincer hydride, (POCOP)Fe(H)(PMe$_3$)$_2$ (**1B**), catalyzing the hydrosilylation reaction with high efficiency.[22] An ionic mechanism that is either similar to that shown in Scheme 3 (in black) or that involves the activation of the initial carbonyl substrate to form η^1- or η^2-carbonyl species,

Scheme 3
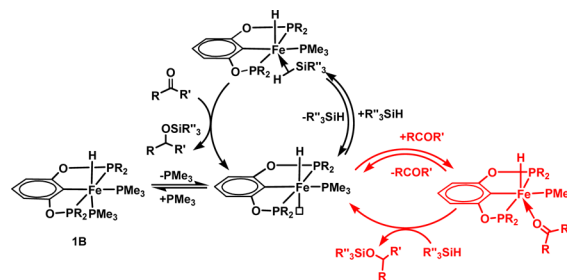
followed by reduction with silane (in red) is proposed to account for the hydrosilylation reaction. In either case, the apical hydride ligand in **1B** is intact during the catalytic cycle. However, direct evidence remains elusive from experimental observations.

The ionic pathway for the hydrosilylation of carbonyl compounds using tris(pentafluorophenyl)borane systems[23,24] has been extensively studied. However, to the best of our knowledge, relatively few theoretical investigations studying a reaction favoring the ionic pathway catalyzed by the transition-metal hydride have been conducted.[25] Therefore, to obtain a clearer understanding of the reactivity of transition-metal complex catalysts in hydrosilylation reactions, particularly those that favor the ionic pathway, we modeled the reactions of the aforementioned POCOP-pincer iridium/iron hydrides **1A-acetone** and **1B** in catalyzing hydrosilylation reactions by using density functional theory.[26] Our objectives are to illustrate the hydrosilylation reaction mechanism catalyzed by POCOP-pincer transition metal Ir(III)/Fe(II) hydrides, to identify the differences in the catalytic cycles that favor the ionic pathway and those that follow the nonionic (carbonyl precoordination) pathway, and to determine the reasons for the differences.

■ COMPUTATIONAL METHODOLOGY

All molecular geometries of the model complexes were optimized at the DFT Becke3LYP (B3LYP)[27] level and by using the hybrid meta exchange-correlation M06 methods,[28] which includes medium-range correlation as implemented in Gaussian 09.[29] For the M06 functional calculation, all geometry optimizations were performed using tight convergence criteria and pruned ultrafine grids. The effective core potentials (ECPs) of Hay and Wadt with double-ζ valence basis sets (LanL2DZ)[30] were used to describe the Ir and Fe metals. In addition, polarization functions were added for Ir ($\zeta_f = 0.938$) and Fe ($\zeta_f = 2.462$).[31] The 6-311g(d,p) basis set was used for all other atoms, such as C, H, P, Si, and O. Frequency calculations at the same level of theory were performed to verify all stationary points as minima (zero imaginary frequency) and transition states (one imaginary frequency), as well as to provide free energies at 298.15 K, including entropic contributions. Selected transition states were verified to connect the respective minima through optimizations following initial intrinsic reaction coordinate calculations.

To obtain the relative solvation-free energies, we used a continuum medium to perform single-point calculations for all of the species under study using the SMD solvation model (an IEFPCM calculation with radii and nonelectrostatic terms for Truhlar and co-workers' SMD solvation model),[32] as implemented in Gaussian 09. CH$_2$Cl$_2$ was used as the solvent. All calculations were performed using the Gaussian 09 software package.

The large butyl/isopropyl groups in the tridentate POCOP-pincer ligands of **1A-acetone** and **1B** were replaced with methyl groups. Benzaldehyde and trimethylsilane were used as model reactants. For intermediates and transition states that have multiple conformations,

several different starting geometries were used to optimize the structures. These structures were then compared to identify the lowest-energy conformation.

The final Gibbs energies (ΔG) reported here are based on B3LYP energies with Gibbs energy corrections (at 298.15 K), solvation corrections, and corrections for dispersion effects using the method of Grimme.[33] The gas-phase Gibbs free energies at the B3LYP-D level are given in parentheses. Inclusion of the dispersion effects improves the performance of the B3LYP method.

In all of our DFT calculations, we used the LanL2DZ ECP basis set, as previously described. Additional calculations that use the triple-ζ SDD[34] basis set with Stuttgart−Dresden ECP for Ir and Fe to calculate the turnover-limiting barriers for the pathways have shown in Figures 3 and 6 that the dependence on the basis set is insignificant. Detailed comparisons of the different basis set levels and functionals (B3LYP, B3LYP-D, and M06) are given in the Supporting Information. The geometries are displayed using CYLview.[35]

■ RESULTS AND DISCUSSION

As previously mentioned, three different reaction pathways are proposed for **1A**- and **1B**-catalyzed hydrosilylation of carbonyl compounds. The first pathway is the ionic hydrosilylation mechanistic pathway (Scheme 2), in which the nucleophilic carbonyl substrates attack the silicon atom in the silane−metal adduct to generate the activated siloxy carbenium ion, which then undergoes the reaction of transferring a hydride from the metal center to the activated siloxy carbenium ion to yield the silyl ether product. The second pathway, called the carbonyl precoordination mechanism, involves the initial coordination of the carbonyl substrate to the metal center, followed by its migratory insertion into the M−H bond to generate the alkoxide intermediate. This intermediate then undergoes σ-bond metathesis of the alkoxy group nucleophilically attacking the silane group to generate the silyl ether product and complete the catalytic cycle. Meanwhile, the third mechanism, which was proposed by Guan and co-workers,[22] involves the formation of η^1- or η^2-carbonyl species followed by reduction with silane (Scheme 3, in red). In the subsequent sections, the analysis results on these reaction pathways as catalyzed by these two POCOP-pincer hydrides (**1A** and **1B**) are presented and discussed in detail.

The same numbering scheme is used for the catalytic cycles with different transition-metal complexes. An explicit reference to an individual system is made by adding **a**/**b** as a suffix: for example, **3a** and **3b** refer to specific examples of intermediate **3**.

Ionic Hydrosilylation Pathway. The ionic hydrosilylation mechanism (Scheme 2) involves three steps: addition of silane to the metal center; transfer of the silyl ion (R_3Si^+) to the carbonyl substrate via the heterolytic cleavage of the Si−H bond, and transfer of the hydride from the transition-metal center to the siloxy carbenium ion to yield the silyl ether product and regenerate the catalyst.

Ionic Hydrosilylation Pathway for 1A-Catalyzed Reaction. The first step of the ionic hydrosilylation pathway involves the coordination of silane to the iridium center in **1A**. This coordination readily occurs to yield (POCOP)Ir(H)(HSiMe$_3$)$^+$ (**3a**). Experimentally, Brookhart[36] characterized the crystal of an η^1-silane iridium complex by X-ray crystallography and showed that the complex exhibits a square-pyramidal structure with an apical hydride and an equatorial η^1-silane ligand. Our DFT-calculated structure for η^1-silane iridium complex **3a** is consistent with the characterized crystal structure (Figure 1). The silane is coordinated *trans* to the *ipso* carbon of the tridentate POCOP backbone, residing on the equatorial
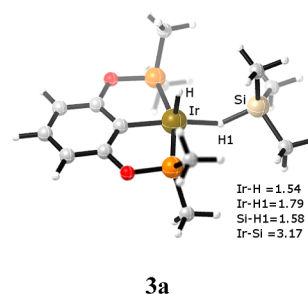

Ir-H = 1.54
Ir-H1 = 1.79
Si-H1 = 1.58
Ir-Si = 3.17

3a

Figure 1. Optimized structure of the η^1-silane iridium complex **3a**.

position. The calculated Ir−H (1.54 Å) and Ir−H1(Si) (1.79 Å) distances are close to those found in the characterized complex (1.43 Å for Ir−H and 1.94 Å for the coordinating Ir−H1(Si) bond). In the optimized structure of **3a**, the Ir···Si distance is significantly long at 3.17 Å, the Ir−H1−Si angle is 141.8°, and the Si−H1 (1.58 Å) distance is slightly longer than that of the free silane molecule (1.49 Å). These results show that the coordination of silane in **3a** is in a much weaker, end-on η^1-H(Si) mode.[37]

The addition of silane to the iridium center in **1A** results in a stabilization energy of 4.3 kcal/mol in the solvent.

Next, a benzaldehyde molecule approaches the η^1-silane iridium complex **3a**. Initially, a loosely bound adduct, **3a +PhCHO**, is formed. In this adduct, the geometries of **3a** and benzaldehyde are barely perturbed from their isolated structures. From the adduct **3a+PhCHO**, taking either H1··· Si or Si···O (PhCHO) separation as the reaction coordinate allows for the location of a transition state (**TS4a_anti**), which corresponds to benzaldehyde nucleophile attacking the silicon center of **3a** in a "back side" manner. This attack represents the *anti* attack of silane by benzaldehyde at the face opposite the metal center.

The transition state **TS4a_anti** exhibits a very late geometry in terms of both short Ir−H1 distance and long Si···H1 separation. In the optimized structure of **TS4a_anti**, the new Ir−H1 bond is fully formed (d(Ir−H1) = 1.66 Å) and is accompanied by a significant elongation of the Si−H1 bond (d(Si···H1) = 2.35 Å). The benzaldehyde substrate is tightly coordinated to the silicon center, with a Si−O distance of 1.91 Å. The coordination geometry around the silicon center is pentacoordinate and can be regarded as a trigonal bipyramid, with the silyl group (SiMe$_3$) acting as the plane and the leaving hydrogen atom and the incoming O (C=O) atom occupying the apical positions. The four atoms Ir···H1···Si···O are roughly in a straight line, with an Ir−H1−Si angle at of 161.5° and an H1−Si−O angle of 177.5°. The calculated vibrational motion of the imaginary frequency associated with **TS4a_anti** represents the expected normal mode of a S_N2-Si reaction, which features the attack of the nucleophilic benzaldehyde group on the silicon center. At the same time, the hydride group moiety leaves the silicon center, which results in the simultaneous cleavage of the Si−H1 bond and formation of the Ir−H1 bond.

The reaction then goes from a complex between two molecular units, **3a** and benzaldehyde substrate, to the siloxy carbenium ion [SiMe$_3$OCHPh]$^+$ paired with the neutral iridium dihydride (POCOP)Ir(H)$_2$, **4a_anti**. In the optimized structure of the intermediate **4a_anti**, the two moieties are largely separated, (d(Si···H1) = 3.20 Å). In addition, the newly formed Ir−H1 bond points toward the unsaturated carbon atom of the
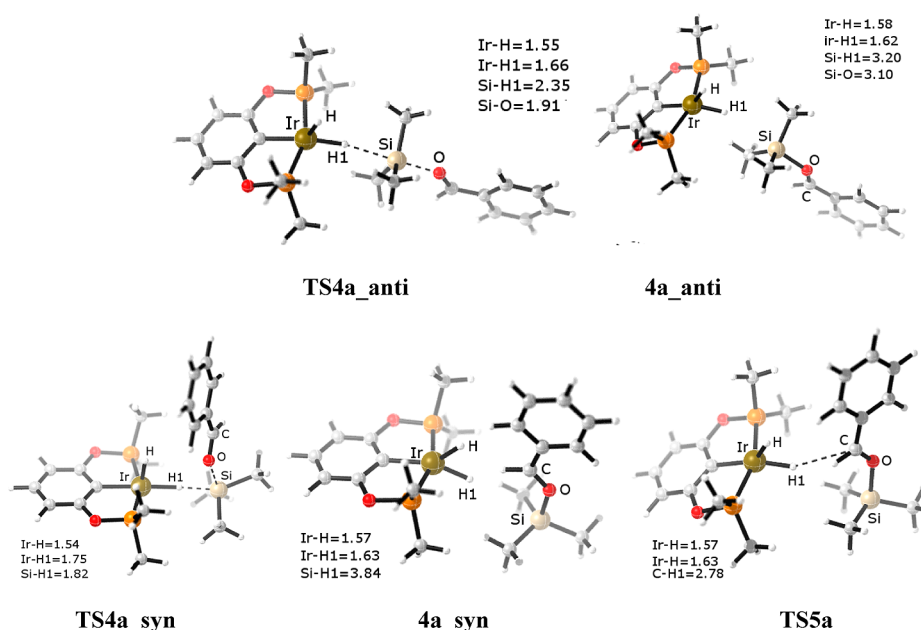
Figure 2. Optimized geometries of **TS4a_anti**, **4a_anti**, **TS4a_syn**, **4a_syn**, and **TS5a** in $(POCOP)Ir(H)^+$ **1A** catalyzed hydrosilylation via the ionic hydrosilylation pathway. The bond distances are shown in Å.

siloxy carbenium ion at a dihedral angle of 155.3°. The optimized structures of the transition state **TS4a_anti** and the intermediate **4a_anti** are shown in Figure 2.

The activation barrier associated with the ionic transition state **TS4a_anti** was calculated as 19.5 kcal/mol relative to the η^1-silane iridium complex **3a**. In addition, the energy of the intermediate **4a_anti** was calculated to be 0.2 kcal/mol below that of **TS4a_anti**. In order to properly describe this ionic process, the transition state **TS4a_anti** and the intermediate **4a_anti** were fully optimized in the solvent. The calculated results give similar Gibbs free energies at the B3LYP-D level of the calculation: 14.5 and 13.3 kcal/mol relative to the isolated reactants **1A** and benzaldehyde and trimethylsilane, respectively. The optimized structures of **TS4a_anti** and **4a_anti** in the solvent are shown in the Supporting Information.

The intermediate **4a_anti** can dissociate to yield the neutral iridium dihydride species $(POCOP)Ir(H)_2$ and the siloxy carbenium ion $[Me_3SiOCHPh]^+$. In addition, the reaction for generation of the isolated neutral iridium dihydride $(POCOP)Ir(H)_2$ and the siloxy carbenium ion $[Me_3SiOCHPh]^+$ from reactant **1A** and trimethylsilane and benzaldehyde

$$\mathbf{1A} + HSiMe_3 + PhCHO$$
$$\rightarrow (POCOP)Ir(H)_2 + SiMe_3OCHPh^+ \qquad (1)$$
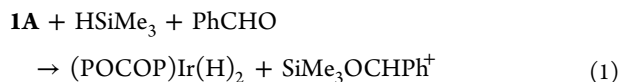
is endoergic, with $\Delta G = 12.5$ kcal/mol. This value is only 2.5 kcal/mol lower than that of **4a_anti**. However, the complete dissociation of **4a_anti** does not constitute an appropriate model for the studied reaction, because the ions are not expected to completely separate from each other in the reaction mixture. Moreover, the driving force for the transfer of a hydride from the neutral iridium dihydride species $(POCOP)Ir(H)_2$ to the siloxy carbenium ion $[Me_3SiOCHPh]^+$ is large

$$(POCOP)Ir(H)_2 + SiMe_3OCHPh^+$$
$$\rightarrow (POCOP)Ir(H)^+ + SiMe_3OCH_2Ph \qquad (2)$$
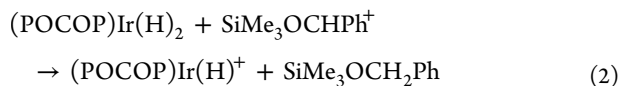
with $\Delta G = -28.3$ kcal. Therefore, a significant accumulation of neutral iridium dihydride is unlikely under the reaction conditions. The catalytic cycle is more likely to proceed without generation of free neutral iridium dihydride or siloxy carbenium ion.

Next, the neutral iridium dihydride $(POCOP)Ir(H)_2$ and the siloxy carbenium ion $[Me_3SiOCHPh]^+$ rearrange to form another isomer, **4a_syn**. In this structure, the reorientation of the silylated benzaldehyde with respect to the metallic fragment results in a *cis* orientation of $[Me_3SiOCHPh]^+$ to the Ir−H1 bond (Figure 2). In other words, benzaldehyde is located around the silicon atom center at the same face as the metal center, in comparison with the *anti* parallel arrangement in **4a_anti**. The geometries of neutral iridium dihydride $(POCOP)Ir(H)_2$ and silylcarbonium ion $[Me_3SiOCHPh]^+$ moieties in **4a_syn** show negligible changes. In addition, this isomerization causes a negligible stabilization of 0.2 kcal/mol.

The next step to complete the catalytic cycle is hydride transfer from the iridium dihydride $(POCOP)Ir(H)_2$ to the siloxy carbenium ion to yield the silyl ether product and regenerate the catalyst. This process readily occurs from the intermediate **4a_syn**. The corresponding transition state **TS5a**, which represents hydride transfer from the iridium center to the C atom in the siloxy carbenium ion group, is located and is associated with a relatively low activation free energy (0.6 kcal/mol). This process is highly exoenergetic, with $\Delta G(\mathbf{4a\_syn} \rightarrow \mathbf{5a}) = -30.6$ kcal/mol.

Alternatively, we found that the intermediate **4a_syn** can be directly generated by "front side" attack of the silicon center by benzaldehyde in **3a**. This represents *syn* attack of silane by benzaldehyde at the same face as the metal center. The transition state (**TS4a_syn**) for such a transformation was determined (Figure 2). In **TS4a_syn**, the silane hydrogen bond is stretched to 1.82 Å and moves close to the iridium center at an Ir···H1 distance of 1.75 Å. The vibrational motion associated with the imaginary frequency represents the simultaneous donation of a hydride by silane to the iridium center and the acceptance of a benzaldehyde oxygen ligand by the $SiMe_3$
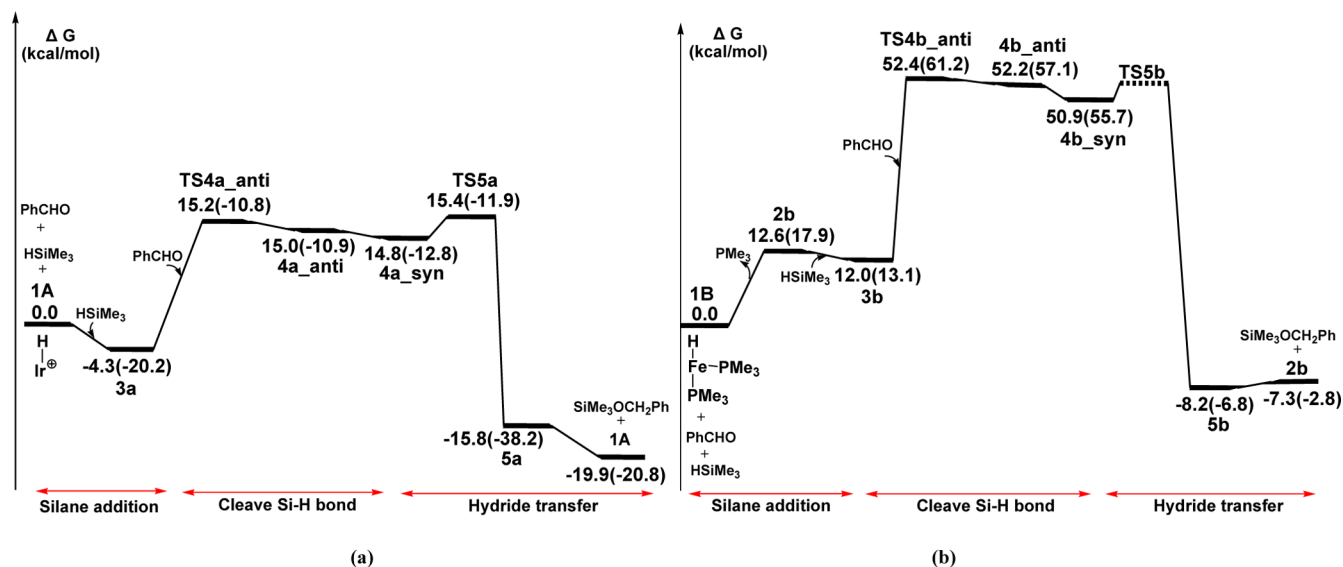
Figure 3. (Schematic free energy surface for (a) **1A**-catalyzed and (b) **1B**-catalyzed hydrosilylation via the ionic hydrosilylation pathway. The solvent-phase Gibbs free energies (ΔG(sol)) are in kcal/mol. Gas-phase free energy results are given in parentheses. Given the large energy barriers obtained, the hydride transfer step **TS5b** was not evaluated.

moiety. However, such an arrangement is expected to be less favorable because of the large steric congestion imposed between benzaldehyde and the methyl groups of the POCOP-pincer ligand. The free energy of **TS4a_syn** is 23.2 kcal/mol, which is 8.0 kcal/mol higher than that of **TS4a_anti**. Therefore, this *syn* arrangement of **TS4a_syn** can be ruled out.

In summary, the calculated free-energy profiles for the ionic hydrosilylation mechanistic pathway complemented with the solvent-phase Gibbs free energy of **1A** with benzaldehyde and trimethylsilane are shown in Figure 3a. The mechanism can be divided into three steps: (1) the addition of silane to the metal center, **1A → 3a**, (2) the heterolytic cleavage of the Si–H bond by nucleophilic attack of benzaldehyde, **TS4a_anti → 4a_anti → 4a_syn**, and (3) hydride transfer, **TS5a → 5a → 1A**. The calculation results indicate that the ionic hydrosilylation pathway is both kinetically and thermodynamically favorable, which is associated with a moderate activation free energy barrier (15.2 kcal/mol, **TS4a_anti**). Along **TS4a_anti → 4a_anti → 4a_syn → TS5a**, the potential energy surface is considerably flat: **4a_syn** is 0.2 kcal/mol more stabilized than **4a_anti**. In addition, a small barrier of 0.6 kcal/mol (**TS5a** relative to **4a_syn**) is required for hydride transfer. These results suggest that through the formation of the ionic transition state **TS4a_anti** and isomerization within the intermediate of **4a_anti** and **4a_syn** the hydride transfer process readily occurs, possibly because of the strong electrostatic attraction between the hydride on the iridium center and the siloxy carbenium carbon atom. Therefore, the turnover-limiting step in the ionic pathway is related to the heterolytic cleavage of the Si–H bond and the hydride transfer step (15.2 and 15.4 kcal/mol above the resting state).

Ionic Hydrosilylation Pathway for 1B-Catalyzed Hydrosilylation. In a similar manner, the ionic mechanism of hydrosilylation of carbonyl compound catalyzed by **1B** was investigated. However, for the reaction to occur, a vacant coordination site must be created to accommodate silane. Therefore, the first step is dissociation of one phosphine ligand from the six-coordinate octahedral structure of **1B**. The calculations show that the resultant (POCOP)Fe(H)(PMe₃)

complex **2b**, in which the PMe₃ ligand *trans* to the apical hydride is dissociated, is 12.6 kcal/mol less stable than **1B**. In contrast, **2bi**, in which PMe₃ *cis* to the hydride ligand is dissociated, is 20.5 kcal/mol less stable than **1B**. Therefore, **2b** is regarded as the starting point in the subsequent discussion of the ionic mechanistic pathway.

From **2b**, addition of free silane generates the η^1-silane iron adduct **3b**, in which the silane is weakly coordinated to the iron center (d(Fe–H1) = 1.81 Å, d(Fe–Si) = 3.24 Å), with a stabilization energy of 0.6 kcal/mol. The structure is shown in the Supporting Information.

Next, the ionic transition states that correspond to the benzaldehyde nucleophilic attack of the silicon atom in the η^1-silane iron adduct were identified. The two ionic transition states in which benzaldehyde attacks *anti* to the silicon center at the face opposite the metal center, **TS4b_anti**, and benzaldehyde attacks *syn* to the silicon center at the face that contains the metal center, **TS4b_syn**, were both located. The optimized structures of **TS4b_anti** and **TS4b_syn** are shown in Figure 4. In **TS4b_anti**, the new Fe–H1 bond is fully formed (d(Fe–H1) = 1.61 Å), whereas the cleavage of the Si–H1 bond is complete (d(Si···H1) = 2.55 Å). The benzaldehyde substrate is tightly coordinated to the silicon center (d(Si–O) = 1.86 Å).
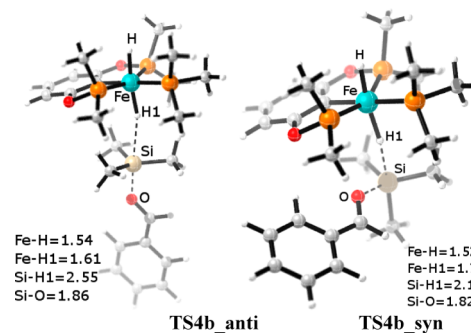
Figure 4. Optimized geometries of the ionic hydrosilylation transition states **TS4b_anti** and **TS4b_syn** in **1B**-catalyzed hydrosilylation via the ionic hydrosilylation pathway. Bond distances are shown in Å.
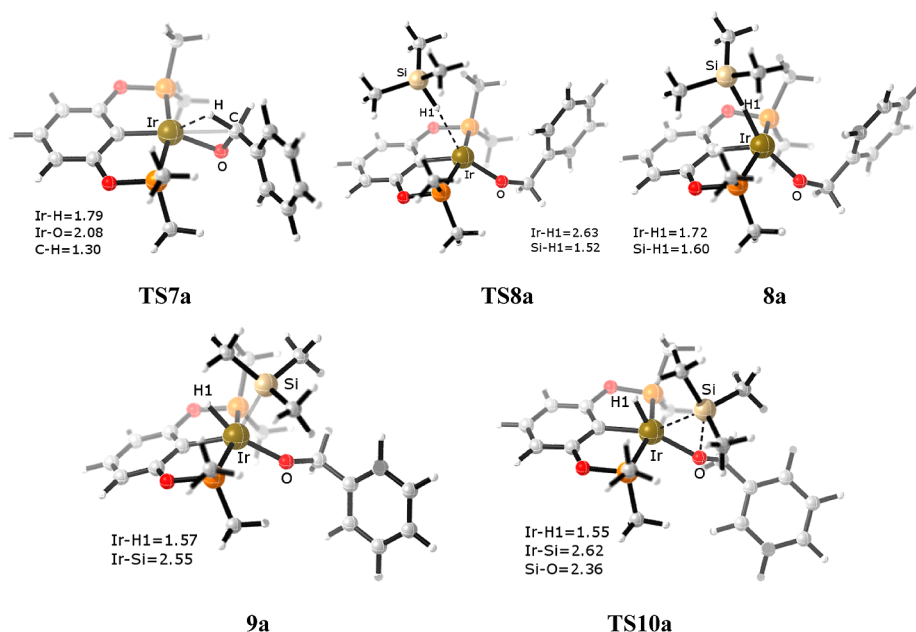
Figure 5. Optimized structures of the **TS7a**, **TS8a**, and **TS10a** transition states and of the **8a** and **9a** intermediates in **1A**-catalyzed hydrosilylation via the carbonyl precoordination pathway. Bond distances are shown in Å.

In **TS4b_syn**, the formation of the Fe−H1 bond, the cleavage of the Si−H1 bond, and the coordination of benzaldehyde to the silicon center occur simultaneously, as indicated by the Fe−H1, Si−H1, and Si−O distances of 1.70, 2.14, and 1.82 Å, respectively.

However, our calculations show that both ionic transition states (**TS4b_anti** and **TS4b_syn**) are highly unstable with respect to catalyst **1B**. Significantly high activation barriers are associated with these two ionic hydrosilylation processes: 52.4 and 56.8 kcal/mol for **TS4b_anti** and **TS4b_syn**, respectively. The free energy profile along the ionic hydrosilylation pathway complemented with the solvent-phase Gibbs free energy of **1B** with benzaldehyde and trimethylsilane is shown in Figure 3b. Thus, given the higher barrier of the ionic transition states, the previously proposed ionic hydrosilylation mechanistic pathway in the iridium hydride is not relevant to the present iron hydride system.

Carbonyl Precoordination Pathway. The ionic hydrosilylation mechanistic pathway described above is for the initial silane activation. However, the possibility of initial carbonyl substrate activation by the catalysts stands. This alternative, which can be called the carbonyl precoordination pathway, was thus investigated. The carbonyl precoordination pathway follows the general path described in other recent computational studies[38] and can be divided into two steps: initial coordination of carbonyl to the metal center and its subsequent migratory insertion into the M−H bond to generate the alkoxide intermediate and silane addition followed by M−O/Si−H metathesis to yield the silyl ether.
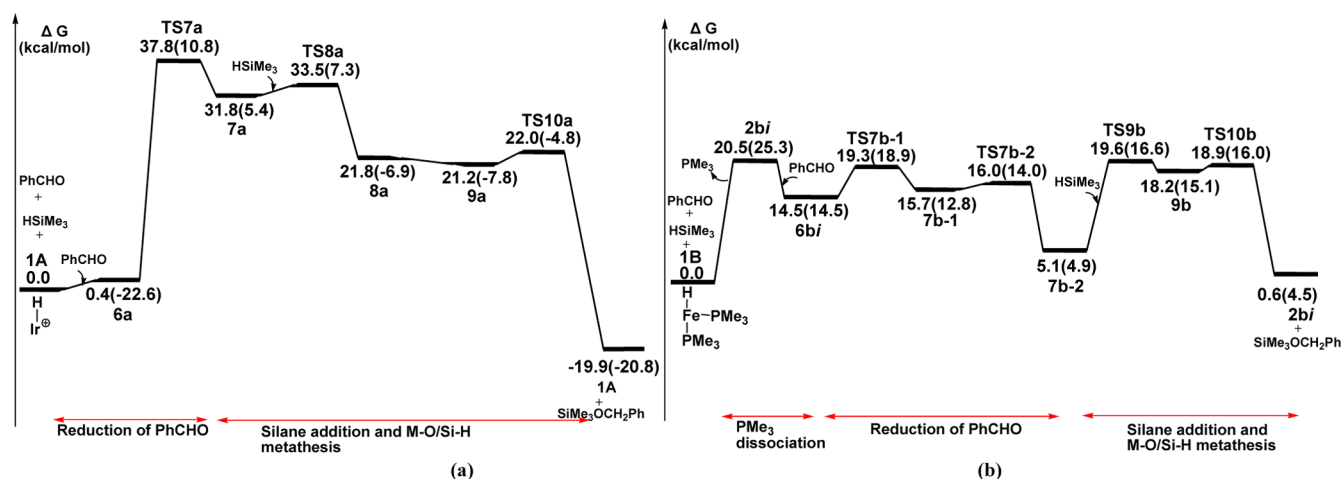
Carbonyl Precoordination Pathway for 1A-Catalyzed Hydrosilylation. The first step of the carbonyl precoordination pathway is coordination of benzaldehyde to the iridium center in **1A** through the oxygen atom (C═O). This coordination yields **6a** (which is the same as **1A**-acetone). In the optimized **6a** structure (shown in the Supporting Information), the Ir−H bond remains untouched (d(Ir−H) = 1.54 Å). The benzaldehyde is bound at the square plane, *trans* to the *ipso* carbon of the tridentate POCOP-pincer backbone. The

structure exhibits a long Ir−O distance of 2.21 Å, a normal C═O bond (1.24 Å), and a long Ir⋯C distance of 3.20 Å, which are indicative of an end-on η^1-carbonyl mode. The benzaldehyde coordination energy of **6a** is slightly endergonic (0.4 kcal/mol).

From η^1-carbonyl complex **6a**, the benzaldehyde C═O bond approaches the iridium center, followed by migratory insertion into the Ir−H bond to afford the alkoxide intermediate. The process was calculated to occur in one concerted process via a four-membered ring that consists of Ir−H and C═O bonds. The corresponding transition state **TS7a** is shown in Figure 5. In the optimized structure of **TS7a**, the apical H atom moves considerably toward the C atom (C═O) and deviates from the apical axis by approximately 58.4°. In addition, the Ir−H distance considerably lengthens to 1.79 Å. The C atom of the C═O bond moves closer to the iridium center and exhibits an η^2-carbonyl mode, with Ir−C and Ir−O distances of 2.40 and 2.08 Å, respectively. The eigenvector with an imaginary frequency in **TS7a** involves Ir−H bond cleavage and C−H bond formation. The insertion product, namely the alkoxide intermediate (POCOP)Ir(OCH$_2$Ph)$^+$ (**7a**), exhibits a distorted, four-coordinate planar structure, with the alkoxide group deviating slightly from the equatorial plane. This migratory insertion was found to require overcoming an overall barrier of 37.8 kcal/mol relative to the reactant **1A** and benzaldehyde. Moreover, the formation of the alkoxide intermediate **7a** is endergonic by as much as 31.8 kcal/mol.

Next, a silane approaches the alkoxide complex **7a** from the apical position and forms (POCOP)Ir(OCH$_2$Ph)(η^1-HSiMe$_3$)$^+$ (**8a**), which has a large stabilization energy of 10.0 kcal/mol. A negligible barrier of 1.7 kcal/mol (**TS8a**) is associated with this process. In the structure of η^1-silane adduct **8a**, the Ir−H1 bond distance is 1.72 Å, the Ir−Si distance is 3.27 Å, and the Ir−H−Si angle is 158.6°. These values indicate that the silane is in an η^1 coordination mode.

The usual feasible reaction followed by the η^1-silane alkoxide adduct **8a** involves an σ-bond metathesis reaction, in which the alkoxide group attacks the silane moiety to generate the silyl

Figure 6. Schematic free energy surface profiles for (a) **1A**- and (b) **1B**-catalyzed hydrosilylation via the carbonyl precoordination pathway. The solvent-phase Gibbs free energies ($\Delta G(sol)$) are in kcal/mol. Gas-phase free energy results are given in parentheses.
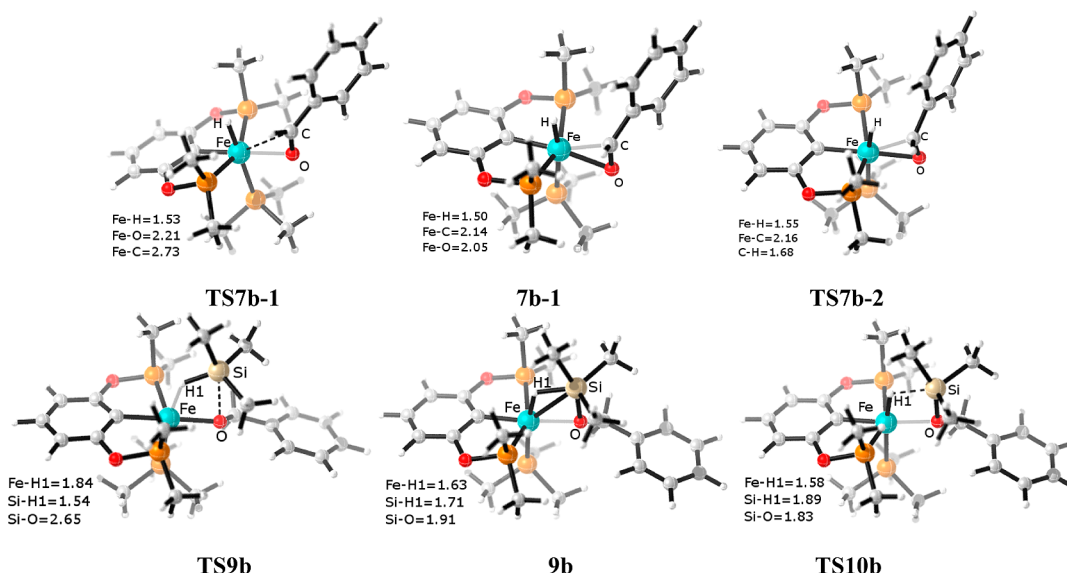
Figure 7. Optimized structures of **TS7b-1**, **TS7b-2**, **TS9b**, **9b**, and **TS10b** for **1B**-catalyzed hydrosilylation via the carbonyl precoordination pathway. Bond distances are shown in Å.

ether product. However, our present DFT calculations show that the η^1-silane in **8a** readily undergoes oxidative addition to the iridium center and forms the thermodynamically slightly preferred isomer (POCOP)Ir(OCH$_2$Ph)(H)(SiMe$_3$)$^+$ (**9a**). A stabilization energy of 0.2 kcal/mol is calculated for the isomerization. In addition, this process proceeds very easily, without the corresponding oxidative addition transition state being located.

In the optimized structure of oxidative addition product **9a**, the silyl group resides between the apical H1 and the alkoxide group with an H1−Ir−Si angle of 68.0°. The apical hydride moiety deviates from the axial axis by approximately 26.2°. The oxidative addition product (POCOP)Ir(OCH$_2$Ph)(H)-(SiMe$_3$)$^+$ (**9a**) then undergoes a three-centered reductive elimination process to afford the silyl ether product. In the located transition state **TS10a**, one imaginary frequency is displayed, the eigenvector of which mainly involves the approach of the Si atom of the silyl group to the O atom of the alkoxide group. The calculated energy barrier for this concerted 1,3-shift transition state (**TS10a**) is negligible (0.8

kcal/mol above that of **9a**). Geometrical optimization from **TS10a** directly leads to the formation of the silyl ether product. The optimized structures of the key intermediate and transition states of the carbonyl precoordination pathway are shown in Figure 5.

In summary, the resulting free energy profiles for **1A**-catalyzed hydrosilylation reaction via the carbonyl precoordination pathway complemented with the solvent-phase Gibbs free energy of **1A** with benzaldehyde and trimethylsilane is shown in Figure 6a and proceeds along **1A** → **6a** → **TS7a** → **7a** → **TS8a** → **8a** → → **9a** → **TS10a** → **1A**. A significantly high activation barrier of 37.8 kcal/mol, which corresponds to the benzaldehyde migratory insertion into the Ir−H bond, must be overcome. The calculated results indicate that the carbonyl substrates are not readily inserted into the Ir−H bond. Therefore, the carbonyl precoordination pathway is not a preferred mechanism for the **1A**-catalyzed hydrosilylation reaction.

*Carbonyl Precoordination Pathway for **1B**-Catalyzed Hydrosilylation.* The migratory insertion step can occur only

when hydride and benzaldehyde are in *cis* positions. Thus, dissociation of phosphine *cis* to the hydride is necessary to generate a vacant site from **1B**. Therefore, **2b*i*** is considered as the starting point in the subsequent discussion of the carbonyl precoordination pathway.

The approach of benzaldehyde to the iron center in **2b*i*** leads to formation of the η^1-carbonyl adduct (POCOP)Fe(H)-(PMe$_3$)(η^1-PhCHO) (**6b*i***), which has a stabilization energy of 6.0 kcal/mol. In **6b*i*** (Supporting Information), the benzaldehyde carbonyl is bound in the equatorial plane, *trans* to the *ipso* carbon of the tridentate POCOP-pincer backbone. The structure exhibits a long Fe−O distance (2.04 Å), a normal C═O bond (1.23 Å), and a long Fe···C distance (2.96 Å), which are characteristic of an end-on η^1-O(carbonyl) mode.

To proceed, benzaldehyde undergoes migratory insertion into Fe−H to generate the alkoxide intermediate. In principle, carbonyl substrates can adopt two fundamental coordination modes in the transition-metal center: end-on coordination (η^1) by a lone pair of the oxygen atom or side-on coordination (η^2) through the C═O π system. Thus, from the η^1-carbonyl complex **6b*i***, the classical reduction in which the carbonyl moiety of benzaldehyde migratorily inserts to the M−H bond to form an alkoxide group can be expected to occur in subsequent steps. The first step involves the change from end-on (η^1) to side-on (η^2) carbonyl coordination. The corresponding transition state is determined as **TS7b-1**, whose Fe−C bond length is shortened to 2.73 Å. This transition state features the moving of the benzaldehyde C atom closer to the iron center, whereas the geometries of other moieties show negligible changes. The transition state **TS7b-1** exhibits one imaginary frequency that involves the approach of the C═O bond to the iron center. In the intermediate **7b-1**, both the O and C atoms in the C═O double bond coordinate with the iron center at an Fe−C distance of 2.14 Å and Fe−O distance of 2.05 Å. These values indicate η^2-carbonyl coordination.

The second step involves the transfer of the hydride on the iron center to the carbonyl substrate. This process indicates that η^2 coordination of the carbonyl undergoes migratory insertion into the Fe−H1 bond. The corresponding transition state is determined as **TS7b-2**. The optimized structures of the transition states **TS7b-1** and **TS7b-2** and of the intermediate **7b-1** are shown in Figure 7. The migratory insertion process was found to involve moderate barriers: 19.3 and 16.0 kcal/mol for **TS7b-1** and **TS7b-2**, respectively. Moreover, the insertion reaction energy is significantly negative (ΔG(**6b*i*** → **7b-2**) = −9.4 kcal/mol). The optimized **7b-2** structure is octahedral, with a vacant site at the apical position of the iron center for further molecular coordination.

Next, a free silane is added to the alkoxide intermediate **7b-2**, generating a η^1-silane alkoxide intermediate. This intermediate then undergoes a Fe−O/Si−H metathesis reaction to afford the silyl ether product and regenerate the catalyst. Given the large steric effect, a stable η^1-silane alkoxide iron complex was not located. As we take the Si···O(OCH$_2$Ph) separation as the reaction coordinate from the precursor complex of **7b-2**+HSiMe$_3$, the metathesis process is actually composed of two consecutive transition states (**TS9b** and **TS10b**), close in energy (19.6 and 18.9 kcal/mol), connecting via a shallow intermediate (**9b**, 18.2 kcal/mol). The first transition state **TS9b** corresponds to bending of the silyl group toward the alkoxide group. In the optimized intermediate **9b**, the H1−Si bond lengthens to 1.71 Å and the Si−O distance shortens to

1.91 Å. The second transition state **TS10b** corresponds to breaking of a Si−H bond and formation of a Si−O bond. In the optimized structure of **TS10b**, the O−Si distance decreases to 1.83 Å, the H1−Si bond significantly lengthens to 1.89 Å, and the Fe−H1 distance shortens to 1.58 Å.

In summary, the computed reaction profile for **1B**-catalyzed hydrosilylation via the carbonyl precoordination pathway is as follows: **1B** → **2b*i*** → **6b*i*** → **TS7b** → **7b-1** → **TS7b-2** → **7b-2** → **TS9b** → **9b** → **TS10b** → **1B**. Figure 6b shows that the overall energies for this path are 20.5, 19.3, and 19.6 kcal/mol, which correspond to the dissociation of the phosphine ligand, the reduction of carbonyl to the alkoxide intermediate, and Fe−O/Si−H metathesis, respectively. Thus, all three steps are considered turnover-limiting steps.

Therefore, in comparison with the ionic pathway discussed previously (Figure 3b), the carbonyl precoordination pathway is the preferred path for **1B**-catalyzed hydrosilylation. The activation energy barrier of the carbonyl precoordination pathway (∼20.0 kcal/mol) is significantly lower than that of the ionic hydrosilylation pathway (52.4 kcal/mol) (Figure 3b). These results indicate that **1B** readily undergoes benzaldehyde migratory insertion into the Fe−H bond to afford the alkoxide intermediate.

Other Possible Reaction Pathways. We also investigated other possible mechanisms for **1B**-catalyzed carbonyl activation, as shown in Scheme 4 (see the Supporting Information for the

Scheme 4

| | **11b (26.1 kcal/mol)** | **12b (30.7 kcal/mol)** |
| **Not located** | | |
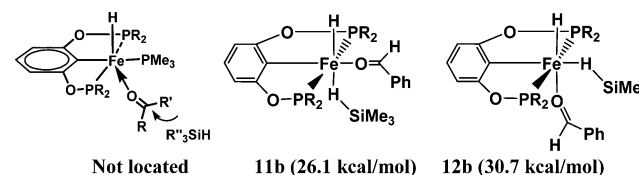
structures of all transition states involved (from **11b** or **12b**) and of POCOP-pincer iridium hydride). First, the possibility of reducing the η^1-carbonyl species **6b** with silane (Scheme 3, in red), as proposed by Guan and co-workers,[22] was examined. However, the formation of such a transition state without dissociation of a second phosphine ligand was not observed.

Alternative paths that involve coordination of another η^1-silane after dissociation of the second phosphine ligand were also investigated. Our calculation results show that such a displacement results in a high destabilization energy (26.1 or 30.7 kcal/mol for **11b** or **12b**, respectively), which is approximately 6.0 kcal/mol higher than that of the turnover-limiting step (∼20.0 kcal/mol) in the carbonyl precoordination pathway (Figure 6b). Thus, the subsequent reaction involving η^1-silane−-η^1-carbonyl intermediate **11b** or **12b** is energetically unfavorable. Therefore, there is a low possibility for overcoming these high barriers, as more competitive pathways are available. In addition, **11b** and **12b** do not contribute to the catalytic activity (**11b** and **12b** transition states are shown in the Supporting Information).

Reasons for the Carbonyl Migratory Insertion of 1B into the Fe−H Bond (but Not of 1A). In the discussion above, we have shown that POCOP-pincer iridium and iron hydrides catalyzed the hydrosilylation of the carbonyl compounds to yield silyl ether products following the ionic hydrosilylation and carbonyl precoordination pathways, respectively. Note that one of the significant differences between

these two reaction pathways by iridium and iron hydrides is in the migratory insertion of the carbonyl substrates. In the present study, our calculations indicate that the activation free energy barrier and reaction free energy values in the insertion of iridium hydride via **6a** → **TS7a** → **7a** are considerably large (37.4 and 31.4 kcal/mol, respectively). However, in the insertion of iron hydride via **6bi** → **TS7b-1** → **7b-1** → **TS7b-2** → **7b-2**, the activation barrier is lower at 4.8 kcal/mol and the reaction free energy is significantly negative at −9.4 kcal/mol. Thus, the geometries of η^1-carbonyl complex **6a** and the transition states **TS7a** and **6bi**, as well as **TS7b-1** and **TS7b-2** (Figure 8), were examined to determine why the reaction at the iridium center is significantly more favorable than that at the iron center.
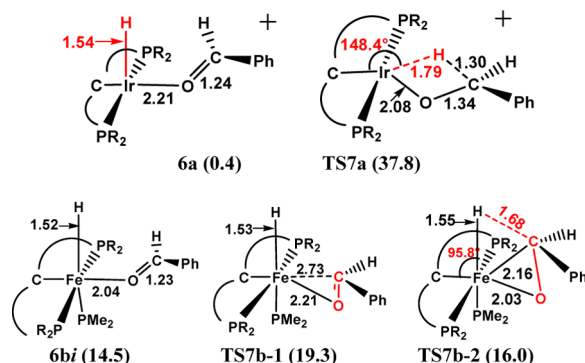
Figure 8. Geometry changes in the migratory insertion steps of **6a** → **TS7a** and **6bi** → **TS7b-1** → **TS7b-2**. Bond distances are in Å.

In the step of carbonyl substrate migratory insertion into the M−H bond, the M−H bond is broken, but C−H bonds are formed. In the transition state **TS7a**, the H−Ir−C(ipso) angle is bent 148.4° toward the C=O bond, thus allowing its approach to the carbon atom of C=O to form a new C−H bond. The Ir−H distance (1.79 Å) is thus distinctively longer than that in the η^1-carbonyl complex **6a** (1.54 Å). Such a significant rearrangement of the apical H ligand results in a considerable geometrical distortion of the Ir−H moiety in **TS7a**, which leads to a high activation barrier (37.4 kcal/mol). However, in the calculated geometries of **TS7b-1** and **TS7b-2**, the distortion of apical hydride units is negligible relative to the calculated free state of η^1-carbonyl complex **6bi**. In addition, the Fe−H distances are only slightly elongated to 1.53 and 1.55 Å in comparison with the 1.52 Å of **6bi**. The bending of the H−Fe−C(ipso) angle is negligible (90.0 and 95.8°). However, the Fe−C(C=O) bond distances are shortened to 2.73 and 2.16 Å, indicating that C=O(benzaldehyde) moves closer to the iron center to allow for the insertion. This phenomenon is associated with a small activation barrier (4.8 kcal/mol).

This high deformation energy associated with the Ir−H moiety in comparison with that of Fe−H can be explained by electron population using NBO analysis. In the η^1-carbonyl complex **6a**, a considerably larger electron population (0.203e) is found in the apical H moiety, whereas a negligible electron population (−0.001e) is found on the apical H in η^1-carbonyl complex **6bi**. These differences are interpreted in terms of a significantly stronger Ir−H bond in comparison with the Fe−H bond, as demonstrated by a Wiberg index (WI) of 0.816 in **6a** in comparison with the 0.775 in **6bi**. This result is expected in terms of bond dissociation energy of the M−H bond, which shows that the Ir−H bond is 12.0 kcal/mol stronger than the

Fe−H bond (see the Supporting Information). Therefore, the bond strengths are responsible for the significantly larger activation barrier associated with benzaldehyde migratory insertion into the Ir−H bond in comparison with that of insertion into the Fe−H bond.

■ CONCLUSIONS

The reaction mechanisms of **1A**- and **1B**-catalyzed hydrosilylation of carbonyl compounds were extensively investigated using DFT calculations. The results show that the reactivities of POCOP-pincer iridium(III) and iron(II) hydrides for carbonyl compound hydrosilylation are significantly different.

(1) For the POCOP-pincer iridium(III) hydride **1A**-catalyzed hydrosilylation reaction via the ionic hydrosilylation pathway, the silane molecule initially coordinates to the iridium center to form the η^1-silane iridium adduct **3a**. Afterward, the benzaldehyde carries out a nucleophilic *anti* attack at the silane center in the η^1-silane iridium adduct **3a**, which results in the heterolytic cleavage of a Si−H bond. Then, the siloxy carbenium ion abstracts hydride on the iridium dihydride to produce the silyl ether product. The calculated energies of the transition states for the heterolytic cleavage of a Si−H bond and the hydride transfer step are nearly identical (15.2 and 15.4 kcal/mol above the resting state); thus it is not evident which one is the turnover-limiting step. In terms of the activation free energy, the ionic hydrosilylation pathway is energetically more favorable than the carbonyl precoordination pathway by as much as 22.6 kcal/mol. This mechanistic proposal is consistent with the experimental observation by Brookhart.[19]

(2) For POCOP-pincer iron(II) hydride **1B**-catalyzed hydrosilylation, our DFT calculations show that the ionic pathway is unlikely because of the extremely high energy barrier (52.4 kcal/mol). However, the reaction proceeds via the initial replacement of carbonyl by a phosphine ligand, followed by its migration insertion into the Fe−H bond to form the alkoxide intermediate. This intermediate then undergoes Fe−O/Si−H σ-bond metathesis to yield the silyl ether product. The ionic hydrosilylation requires an activation energy that is ∼30.0 kcal/mol higher than that of the carbonyl precoordination pathway.

We would like to emphasize the following points: (1) the apical hydride is not involved in POCOP-pincer iridium(III) hydride **1A**-catalyzed catalytic hydrosilylation of carbonyl compounds but is involved in the POCOP-pincer iron(II) hydride **1B**-catalyzed reaction and (2) the POCOP-pincer iridium(III) hydride complex **1A** is unique with regard to activating the Si−H bonds in an ionic manner. The requirement of carbonyl coordination and insertion in such an ionic mechanism is removed, thus broadening the range of transition metals that can be used. Our calculations on the two POCOP-pincer transition metal hydrides may also be considered to model the action of a series of transition-metal hydride catalysts. Further studies may ultimately lead to the design of more efficient catalysts that favor the ionic mechanism on the basis of the mechanistic understanding gained in this study.

■ ASSOCIATED CONTENT

Ⓢ Supporting Information

Text, tables, and figures giving the complete ref 29, a comparison of different basis set levels and methods (B3LYP, B3LYP-D, and M06), additional results not shown in the text, and Cartesian coordinates of all optimized structures discussed

in the paper. This material is available free of charge via the Internet at http://pubs.acs.org.

■ AUTHOR INFORMATION

Corresponding Author
*E-mai for H.W.: weihaiyan@njnu.edu.cn.

Notes
The authors declare no competing financial interest.

■ REFERENCES

(1) Sark, N.; Bruno, J. W. *J. Am. Chem. Soc.* **1999**, *121*, 2174.
(2) Darensbourg, M. Y.; Ash, C. E. *Adv. Organomet. Chem.* **1987**, *27*, 1.
(3) Parshall, G. W.; Ittel, S. D. *Homogeneous Catalysis*, 2nd ed.; Wiley: New York, 1992.
(4) (a) Hembre, R. T.; McQueen, S. *J. Am. Chem. Soc.* **1994**, *116*, 2141. (b) Hembre, R. T.; McQueen, J. S. *Angew. Chem., Int. Ed. Engl.* **1997**, *36*, 65.
(5) Bunting, J. W. *Bioorg. Chem.* **1991**, *19*, 456.
(6) (a) Kreevoy, M. M.; Kotchevar, A. T. *J. Am. Chem. Soc.* **1990**, *112*, 3579. (b) Kreevoy, M. M.; Ostovic, D.; Lee, I.-S. H.; Binder, D. A.; King, G. W. *J. Am. Chem. Soc.* **1988**, *110*, 524. (c) Lee, I.-S. H.; Ostovic, D.; Kreevoy, M. *J. Am. Chem. Soc.* **1988**, *110*, 3989.
(7) Labinger, J. A.; Komadina, K. H. *J. Organomet. Chem.* **1978**, *155*, C25.
(8) Mock, M. T.; Potter, R. G.; Camaioni, D. M.; Li, J. *J. Am. Chem. Soc.* **2009**, *131*, 14454.
(9) (a) Bolm, C.; Legros, J.; Le Paih, J.; Zani, L. *Chem. Rev.* **2004**, *104*, 6217. (b) Morris, R. H. *Chem. Soc. Rev.* **2009**, *38*, 2282. (c) Junge, K.; Schröder, K.; Beller, M. *Chem. Commun.* **2011**, *47*, 4849.
(10) (a) Chalk, A. J.; Harrod, J. F. *J. Am. Chem. Soc.* **1965**, *87*, 16. (b) Ojima, I.; Nihonyanagi, M.; Nagai, Y. *J. Chem. Soc., Chem. Commun.* **1972**, 938. (c) Ojima, I.; Nihonyanagi, M.; Kogure, T.; Kumagai, M.; Horiuchi, S.; Nakatsugawa, K.; Nagai, Y. *J. Organomet. Chem.* **1975**, *94*, 449. (d) Kobayashi, M.; Koyama, T.; Ogura, K.; Seto, S.; Ritter, F. J.; Brueggemann-Rotgans, I. E. M. *J. Am. Chem. Soc.* **1980**, *102*, 6602. (e) Semmelhack, M. F.; Misra, R. N. *J. Org. Chem.* **1982**, *47*, 2469. (f) Ojima, I.; Kogure, T. *Organometallics* **1982**, *1*, 1390.
(11) (a) Brunner, H.; Becker, R.; Riepl, G. *Organometallics* **1984**, *3*, 1354. (b) Ohkuma, T.; Hashiguchi, S.; Noyori, R. *J. Org. Chem.* **1994**, *59*, 217. (c) Zheng, G. Z.; Chan, T. H. *Organometallics* **1995**, *14*, 70. (d) Wright, M. E.; Cochran, B. B. *Organometallics* **1996**, *15*, 317. (e) Nagashima, H.; Suzuki, A.; Iura, T.; Ryu, K.; Matsubara, K. *Organometallics* **2000**, *19*, 3579.
(12) (a) Kennedy-Smith, J. J.; Nolin, K. A.; Gunterman, H. P.; Toste, F. D. *J. Am. Chem. Soc.* **2003**, *125*, 4056.
(13) (a) Reis, P. M.; Romão, C. C.; Royo, B. *Dalton Trans.* **2006**, 1842. (b) Noronha, R. G.; Costa, P. G.; Calhorda, M. J.; Romão, C. C.; Fernandes, A. C. *Organometallics* **2009**, *28*, 6206. (c) Calhorda, M. J.; Costa, P. J. *Dalton Trans.* **2009**, 8155.
(14) (a) Du, G. D.; Fanwick, P. E.; Abu-Omar, M. M. *J. Am. Chem. Soc.* **2007**, *129*, 5180. (b) Ison, E. A.; Corbin, R. A.; Abu-Omar, M. M. *J. Am. Chem. Soc.* **2005**, *127*, 11938. (c) Ison, E. A.; Trivedi, E. R.; Corbin, R. A.; Abu-Omar, M. M. *J. Am. Chem. Soc.* **2005**, *127*, 15374.

(d) Fernandes, A. C.; Fernandes, R; Romão, C. C.; Royo, B. *Chem Commun.* **2005**, 213. (e) Kühn, F. E.; Herdtweck, E.; Haider, J. J.; Herrmann, W. A.; Goncalves, I. S.; Romão, C. C. *J. Organomet. Chem.* **1999**, *583*, 3. (f) Abrantes, M.; Santos, A. M.; Mink, J.; Kühn, F. E.; Romão, C. C. *Organometallics* **2003**, *22*, 2112. (g) Fernandes, A. C.; Fernandes, J. A.; Romão, C. C.; Veiros, L. F.; Calhorda, M. J. *Organometallics* **2010**, *29*, 5517. (h) Peterson, E.; Khalimon, A. Y.; Simionescu, R.; Kuzmina, L. G.; Howard, J. A. K.; Nikonov, G. I. *J. Am. Chem. Soc.* **2009**, *131*, 908.
(15) (a) Nolin, K. A.; Krumper, J. R.; Pluth, M. D.; Bergman, R. G.; Toste, F. D. *J. Am. Chem. Soc.* **2007**, *129*, 14684. (b) Chung, L. W.; Lee, H. G.; Wu, Y. W. *J. Org. Chem.* **2006**, *71*, 6000. (c) Costa, P. J.; Romão, C. C.; Fernandes, A. C.; Roya, B.; Reis, P. M.; Calhorda, M. J. *Chem. Eur. J.* **2007**, *13*, 3934. (d) Markus, D.; Strassner, T. *Inorg. Chem.* **2007**, *46*, 10850. (e) Johnson, M. T.; Johansson, R.; Kondrashov, M. V.; Steyl, G.; Ahlquist, M. S. G.; Roodt, A.; Wendt, O. F. *Organometallics* **2010**, *29*, 3521.
(16) (a) Bullock, R. M. *Chem. Eur. J.* **2004**, *10*, 2366. (b) Bullock, R. M.; Rappoli, B. J. *J. Chem. Soc., Chem. Commun.* **1989**, 1447. (c) Bullock, R. M.; Song, J.-S. *J. Am. Chem. Soc.* **1994**, *116*, 8602. (d) Luan, L.; Song, J.-S.; Bullock, R. M. *J. Org. Chem.* **1995**, *60*, 7170. (e) Gaus, P. L.; Kao, S. C.; Youngdahl, K.; Darensbourg, M. Y. *J. Am. Chem. Soc.* **1985**, *107*, 2428.
(17) (a) Shirobokov, O. G.; Kuzmina, L. G.; Nikonov, G. I. *J. Am. Chem. Soc.* **2011**, *133*, 6487. (b) Khalimon, A. Y.; Ignatov, S. K.; Simionescu, R.; Kuzmina, L. G.; Howard, J. A. K.; Nikonov, G. I. *Inorg. Chem.* **2012**, *51*, 754. (c) Khalimon, A. Y.; Shirobokov, O. G.; Peterson, E.; Simionescu, R.; Kuzmina, L. G.; Howard, J. A. K.; Nikonov, G. I. *Inorg. Chem.* **2012**, *51*, 4300. (d) Peterson, E.; Khalimon, A. Y.; Simionescu, R.; Kuzmina, L. G.; Howard, J. A. K.; Nikonov, G. I. *J. Am. Chem. Soc.* **2009**, *131*, 908. (e) Ignatov, S. K.; Rees, N. H.; Merkoulov, A. A.; Dubberley, S. R.; Razuvaev, A. G.; Mountford, P.; Nikonov, G. I. *Organometallics* **2008**, *27*, 5968.
(18) (a) Gibson, D. H.; El-Omrani, Y. S. *Organometallics* **1985**, *4*, 1473. (b) Song, J.-S.; Szalda, D. J.; Bullock, R. M.; Lawrie, C. J. C.; Rodkin, M. A.; Norton, J. R. *Angew. Chem.* **1992**, *104*, 1280. (c) Song, J.-S.; Szalda, D. J.; Bullock, R. M. *Organometallics* **2001**, *20*, 3337. (d) Song, J.-S.; Szalda, D. J.; Bullock, R. M. *Inorg. Chim. Acta* **1997**, *259*, 161. (e) Song, J.-S.; Szalda, D. J.; Bullock, R. M. *J. Am. Chem. Soc.* **1996**, *118*, 11134.
(19) Park, S.; Brookhart, M. *Organometallics* **2010**, *29*, 6057.
(20) (a) Parks, D. J.; Blackwell, J. M.; Piers, W. E. *J. Org. Chem.* **2000**, *65*, 3090. (b) Parks, D. J.; Piers, W. E. *J. Am. Chem. Soc.* **1996**, *118*, 9440. (c) Parks, D. J.; Piers, W. E.; Parvez, M.; Atencio, R.; Zaworotko, M. J. *Organometallics* **1998**, *17*, 1369. (d) Blackwell, J. M.; Sonmor, E. R.; Scoccitti, T.; Piers, W. E. *Org. Lett.* **2000**, *2*, 3921. (e) Berkefeld, A.; Piers, W. E.; Parvez, M. *J. Am. Chem. Soc.* **2010**, *132*, 10660. (f) Tutusaus, O.; Chengbao, N.; Szymczak, N. K. *J. Am. Chem. Soc.* **2013**, *135*, 3403. (g) Bertini, F.; Lyaskovskyy, V.; Timmer, B. J. J.; Lutz, M.; Ehlers, A. W.; Slootweg, J. C.; Lammertsma, K. *J. Am. Chem. Soc.* **2012**, *134*, 201. (h) Chapman, A. M.; Haddow, M. F.; Wass, D. F. *J. Am. Chem. Soc.* **2011**, *133*, 18463. (i) Xiaoxi, Z.; Stephan, D. W. *J. Am. Chem. Soc.* **2011**, *133*, 12448. (j) Geier, S. J.; Stephan, D. W. *J. Am. Chem. Soc.* **2009**, *131*, 3476.
(21) (a) Dioumaev, V. K.; Bullock, R. M. *Nature* **2003**, *424*, 530. (b) Gutsulyak, D. V.; Vyboishchikov, S. F.; Nikonov, G. I. *J. Am. Chem. Soc.* **2010**, *132*, 5950. (c) Bullock, R. M.; Voges, M. H. *J. Am. Chem. Soc.* **2000**, *122*, 12594. (d) Voges, M. H.; Bullock, R. M. *Dalton Trans.* **2002**, 759. (e) Bernskoetter, W. H.; Hanson, S. K.; Brookhart, M. *J. Am. Chem. Soc.* **2009**, *131*, 8603. (f) Park, S.; Brookhart, M. *J. Am. Chem. Soc.* **2012**, *134*, 640. (g) Yang, J.; White, P. S.; Brookhart, M. *J. Am. Chem. Soc.* **2008**, *130*, 17509. (h) Findlater, M.; Bernskoetter, W. H.; Brookhart, M. *J. Am. Chem. Soc.* **2010**, *132*, 4534. (i) Park, S.; Brookhart, M. *Chem. Commun.* **2011**, *47*, 3643. (j) Yang, J.; Brookhart, M. *Adv. Synth. Catal.* **2009**, *351*, 175. (k) Yang, J.; Brookhart, M. *J. Am. Chem. Soc.* **2007**, *129*, 12656. (l) Park, S.; Bezier, D.; Brookhart, M. *J. Am. Chem. Soc.* **2012**, *134*, 11404. (m) Bezier, D.; Park, S.; Brookhart, M. *Org. Lett.* **2013**, *15*, 496.

(22) Bhattacharya, P.; Krause, J. A.; Guan, H. *Organometallics* **2011**, *30*, 4720.

(23) (a) Dureen, M. A.; Stephan, D. W. *J. Am. Chem. Soc.* **2009**, *131*, 8396. (b) Rokob, T. A.; Hamza, A.; Stirling, A.; Păpai, I. *J. Am. Chem. Soc.* **2009**, *131*, 2029. (c) Berkefeld, A.; Piers, W. E.; Parvez, M. *J. Am. Chem. Soc.* **2010**, *132*, 10660. (d) Momming, C. M.; Fromel, S.; Kehr, G.; Frohlich, R.; Grimme, S.; Erker, G. *J. Am. Chem. Soc.* **2009**, *131*, 12280.

(24) (a) Yanfeng, J.; Blacque, O.; Fox, T.; Berke, H. *J. Am. Chem. Soc.* **2013**, *135*, 7751. (b) Ménard, G.; Hatnean, J. A.; Cowley, H. J.; Lough, A. J.; Rawson, J. M.; Stephan, D. W. *J. Am. Chem. Soc.* **2013**, *135*, 6446. (c) Rokob, T. A.; Bakó, I.; Stirling, A.; Hamza, A.; Pápai, I. *J. Am. Chem. Soc.* **2013**, *135*, 4425. (d) Piao, G.; Wenmin, W.; Yiou, W.; Haiyan, W. *Organometallics* **2013**, *32*, 47.

(25) (a) Gutsulyak, D. V.; Vyboishchikov, S. F.; Nikonov, G. I. *J. Am. Chem. Soc.* **2010**, *132*, 5950. (b) Nagaraja, C. M.; Parameswaran, P.; Jemmis, E. D.; Jagirdar, B. R. *J. Am. Chem. Soc.* **2007**, *129*, 5587. (c) Bühl, M.; Mauschick, F. T. *Organometallics* **2003**, *22*, 1422. (d) Namorado, S.; Antunes, M. A.; Veiros, L. F.; Ascenso, J. R.; Duarte, M. T.; Martins, A. M. *Organometallics* **2008**, *27*, 4589.

(26) Parr, R. G.; Yang, W. *Density Functional Theory of Atoms and Molecules*; Oxford University Press: New York, 1989.

(27) (a) Becke, A. D. *J. Chem. Phys.* **1993**, *98*, 5648. (b) Lee, C.; Yang, W.; Parr, R. G. *Phys. Rev. B* **1988**, *37*, 785. (c) Miehlich, B.; Savin, A.; Stoll, H.; Preuss, H. *Chem. Phys. Lett.* **1989**, *157*, 200. (d) Stephens, P. J.; Devlin, F. J.; Chaobalowski, C. F. *J. Phys. Chem.* **1994**, *98*, 11623. (e) Krishnan, R.; Binkley, J. S.; Seeger, R.; Pople, J. A. *J. Chem. Phys.* **1980**, *72*, 650.

(28) (a) Yan, Z.; Truhlar, D. G. *J. Phys. Chem. A* **2008**, *112*, 6794. (b) Denis, J.; Eric, A.; Carlo, A.; Rosendo, V.; Yan, Z.; Truhlar, D. G. *J. Chem. Theory Comput.* **2010**, *6*, 2071. (c) Faza, O. N.; Rodriguez, R. Á.; Lopez, C. S. *Theor. Chem. Acc.* **2011**, *128*, 647.

(29) Frisch, M. J., et al. *Gaussian 09, Revision A.02*; Gaussian, Inc., Wallingford, CT, 2009.

(30) (a) Hay, P. J.; Wadt, W. R. *J. Chem. Phys.* **1985**, *82*, 299. (b) Wadt, W. R.; Hay, P. J. *J. Chem. Phys.* **1985**, *82*, 284.

(31) (a) Ehlers, A. W.; Böhme, M.; Dapprich, S.; Gobbi, A.; Hoöllwarth, A.; Jonas, V.; Koöhler, K. F.; Stegmenn, R.; Frenking, G. *Chem. Phys. Lett.* **1993**, *208*, 111. (b) Hoöllwarth, A.; Boöhme, M.; Dapprich, S.; Ehlers, A. W.; Gobbi, A.; Jonas, V.; Koöhler, K. F.; Stegmenn, R.; Veldkamp, A.; Frenking, G. *Chem. Phys. Lett.* **1993**, *208*, 237.

(32) Marenich, A. V.; Cramer, C. J.; Truhlar, D. G. *J. Chem. Phys. B* **2009**, *113*, 6378.

(33) (a) Grimme, S. *J. Comput. Chem.* **2006**, *27*, 1787. (b) Kryspin, I. H.; Grimme, S. *Organometallics* **2009**, *28*, 1001. (c) Grimme, S. *J. Chem. Phys.* **2006**, *124*, 034108. (d) Grimme, S. *J. Comput. Chem.* **2004**, *25*, 1463. (e) Schwabe, T.; Grimme, S. *Phys. Chem. Chem. Phys.* **2007**, *9*, 3397.

(34) (a) Dolg, M.; Wedig, U.; Stoll, H.; Preuss, H. *J. Chem. Phys.* **1987**, *86*, 866. (b) Andrae, D.; Haussermann, U.; Dolg, M.; Stoll, H.; Preuss, H. *Theor. Chim. Acta.* **1990**, *77*, 123.

(35) Legault, C. Y. *CYLview, 1.0b*; Université de Sherbrooke, 2009; http://www.cylview.org.

(36) Yang, J.; White, P. S.; Schauer, C. K.; Brookhart, M. *Angew. Chem., Int. Ed.* **2008**, *47*, 4141.

(37) Brookhart has also calculated the η^1-silane Ir(III) complex with the iPr-substituted POCOP ligand. Our calculations on the model (Me-substituted POCOP ligand) are consistent with those for the iPr-substituted POCOP ligand η^1-silane Ir(III) complex, with an Ir–H distance of 1.54 Å vs 1.53 Å, an Si–H distance of 1.58 Å vs 1.57 Å, and an Ir–H distance of 1.79 Å vs 1.86 Å.

(38) (a) Clapham, S. E.; Hadzovic, A.; Morris, R. H. *Coord. Chem. Rev.* **2004**, *248*, 2201. (b) Chakraborty, S.; Guan, H. *Dalton Trans.* **2010**, *39*, 7427.